Order by disorder and spiral spin liquid in
frustrated diamond lattice antiferromagnets

Doron Bergman[*,1] Jason Alicea,[1] Emanuel Gull,[2] Simon Trebst,[3] and Leon Balents[1]

[1]*Department of Physics, University of California, Santa Barbara, CA 93106-9530*
[2]*Theoretische Physik, Eidgenössische Technische Hochschule Zürich, CH-8093 Zürich, Switzerland*
[3]*Microsoft Research, Station Q, University of California, Santa Barbara, CA 93106*
(Dated: November 30, 2006)

Frustration refers to competition between different interactions that cannot be simultaneously satisfied, a familiar feature in many magnetic solids. Strong frustration results in highly degenerate ground states, and a large suppression of ordering by fluctuations. Key challenges in frustrated magnetism are characterizing the fluctuating *spin-liquid* regime and determining the mechanism of eventual order at lower temperature. Here, we study a model of a diamond lattice antiferromagnet appropriate for numerous spinel materials. With sufficiently strong frustration a massive ground state degeneracy develops amongst spirals whose propagation wavevectors reside on a continuous two-dimensional "spiral surface" in momentum space. We argue that an important ordering mechanism is *entropic* splitting of the degenerate ground states, an elusive phenomena called *order-by-disorder*. A broad "spiral spin-liquid" regime emerges at higher temperatures, where the underlying spiral surface can be directly revealed via spin correlations. We discuss the agreement between these predictions and the well characterized spinel $MnSc_2S_4$.

PACS numbers:

When microscopic interactions in a material conspire to "accidentally" produce many nearly degenerate low-energy states, otherwise weak residual effects can give rise to remarkable emergent behavior. This theme recurs throughout modern condensed matter physics. Quintessential examples include the cuprates, with several competing orders including high-T_c superconductivity, and exotic quantum (Hall) liquids in two-dimensional electron systems, arising from partial Landau-level occupation. Insulating magnets constitute a particularly abundant source of such phenomena, as in numerous cases *frustration* generated by the competition between different exchange interactions leads to large classical ground-state degeneracies. An important experimental signature of such degeneracies is an anomalously low ordering temperature T_c relative to the Curie Weiss temperature Θ_{CW}; indeed, values of the "frustration parameter" $f = |\Theta_{CW}|/T_c$ larger than 5-10 are typically taken as empirical evidence of a highly frustrated magnet.[1] This sharp suppression of T_c opens up a broad "spin-liquid" regime for temperatures $T_c \lesssim T \lesssim |\Theta_{CW}|$, where the system fluctuates amongst the many low-energy configurations but evades long-range order. Highly non-trivial physics can emerge here, as attested for instance in pyrochlore antiferromagnets by the experimental observation of hexagonal loop correlations in neutron scattering on the spinel $ZnCr_2O_4$[2], and theoretically by the establishment of "dipolar" correlations.[3]

Low-temperature ordering in highly frustrated magnets often displays an exquisite sensitivity to degeneracy-breaking perturbations, notably dipolar interactions and minimal disorder in the spin-ice pyrochlores,[4], spin-lattice coupling in various spinels[5], and Dzyaloshinskii-Moriya interactions in Cs_2CuCl_4[6]. However, the lifting of degeneracy need not require the presence of such explicit perturbations. This can be achieved, rather remarkably, by *fluctuations* – a process commonly referred to as "order-by-disorder".[7] Here, degeneracy in the free energy is lifted *entropically*, resulting in ordering which counter-intuitively is enhanced by increasing temperature. An analogous phenomenon occurs in quantum spin models at $T = 0$, where quantum fluctuations provide the degeneracy-breaking mechanism [8, 9, 10]. Whether or not order-by-disorder transpires depends crucially upon the degree of degeneracy: it is known to occur in various FCC antiferromagnets[11, 12], for instance, but not in the more severely degenerate nearest-neighbor pyrochlore antiferromagnet[13, 14], where instead a classical spin-liquid regime extends down to $T = 0$. While these ideas have existed for decades and enjoy broad acceptance in the theoretical community, compelling experimental evidence for order-by-disorder in even one example is presently lacking.

Here we argue that entropic effects may play a key role in the physics of insulating normal spinels, with the generic chemical formula AB_2X_4, that comprise antiferromagnets on a *diamond* lattice formed by magnetic, orbitally non-degenerate A sites (see Fig. 1). Numerous strongly frustrated materials in this class have been recent subjects of intensive experimental study; in particular, $CoAl_2O_4$ and $MnSc_2S_4$ for which $f > 10 - 20$ [15, 16] and $f \approx 10$ [17], respectively, are expected to provide ideal test grounds for the physics we describe. We introduce a simple classical model for these materials, consisting of a basic "parent" Hamiltonian supplemented by small corrections, that exhibits complex behavior in accord with numerous experimental observations. Remarkably, ground states of the parent theory are (for most of its phase space) highly degenerate coplanar spirals, whose propagation wavevectors form a *continuous surface* in momentum space. Within our parent theory, order-by-disorder occurs with a dramatically suppressed T_c relative to Θ_{CW}, and above T_c a "spiral spin liquid" regime emerges where the system fluctuations among these degenerate spirals. While the small corrections (which we describe) inevitably determine

specific ground states at the lowest temperatures, entropy washes these out at higher temperatures, allowing the spiral spin liquid and/or order-by-disorder physics inherent to the parent Hamiltonian to become visible. This energy-entropy competition is thus manifest as an interesting multi-stage ordering behavior.

Superficially, the strong frustration inherent in materials such as $MnSc_2S_4$ seems rather puzzling. Indeed, the diamond lattice is bipartite, and accordingly a model with only nearest-neighbor spin coupling J_1, whether ferromagnetic or antiferromagnetic, exhibits *no* frustration. Additional interactions must therefore be incorporated to account for the observed frustration. We first consider the simplest modification that achieves this, and assume a Hamiltonian with additional second-neighbor antiferromagnetic exchange J_2:

$$H = J_1 \sum_{\langle ij \rangle} \mathbf{S}_i \cdot \mathbf{S}_j + J_2 \sum_{\langle\langle ij \rangle\rangle} \mathbf{S}_i \cdot \mathbf{S}_j. \tag{1}$$

Here the spins $\mathbf{S}_i$ are modeled as classical three-component unit vectors (absorbing a factor of $S(S+1)$ into the definition of J_i), appropriate to the large spin values ($S = 3/2, 5/2$) for these materials. Throughout we set the lattice constant $a = 1$ and consider $J_2 > 0$ appropriate for antiferromagnetic exchange. While the sign of J_1 can always be changed by sending $\mathbf{S}_i \to -\mathbf{S}_i$ on one of the two diamond sublattices, for ease of discussion we will assume antiferromagnetic $J_1 > 0$ unless specified otherwise. Additional interactions such as further-neighbor exchange may also be present, but will be assumed small and returned to only at the end of the paper. As we will see, the parent Hamiltonian Eq. (1) leads to a rich theoretical picture which we argue captures the essential physics operating in these strongly frustrated materials.

To appreciate the frustration in H, it is convenient to view the diamond lattice as composed of two interpenetrating FCC sublattices (colored orange and green in Fig. 1). From this perspective, J_1 couples the two FCC sublattices, while J_2 couples nearest-neighbors *within* each FCC sublattice. The FCC antiferromagnet is known to be highly frustrated,[18] and hence J_2 generates strong frustration which the competition from J_1 further enhances. In fact, as argued long ago [19] and emphasized in [17, 20], due to the similarity in exchange paths coupling first- and second-neighbor sites in such materials, J_1 and J_2 are generally expected to have comparable strengths.

We begin by discussing the zero-temperature properties of Eq. (1). Exact ground states can be obtained for arbitrary J_2/J_1. In the weakly frustrated limit with $0 \leq J_2/J_1 \leq 1/8$, the ground state is the Néel phase, with each spin anti-aligned with those of its nearest neighbors. For larger J_2 the simple Néel phase is supplanted by a massively degenerate set of coplanar spin spirals. As described above, and illustrated schematically in Fig. 1, each spiral ground state is characterized by a single wavevector $\mathbf{q}$ lying on a two-dimensional "spiral surface". This surface possesses a nearly spherical geometry for coupling strengths $1/8 < J_2/J_1 < 1/4$, and exhibits an open topology for $J_2/J_1 > 1/4$ where it develops "holes" centered around the (111)-directions (see Fig. 2). In the limit $J_2/J_1 \to \infty$, the surface collapses into one-dimensional lines, which are known to characterize the ground states of the nearest-neighbor-coupled FCC antiferromagnet.[18]

At small but non-zero temperature, one must consider both the local stability and the global selection amongst these ground states. The stability issue is quite delicate, since at $T = 0$ the spins can smoothly distort from one ground state to any other at no energy cost. More formally, for any ground state at $T = 0$ there is a branch of normal modes whose frequencies $\omega_0(\mathbf{q})$ have an infinite number of zeros, vanishing for any $\mathbf{q}$ on the spiral surface. This leads to a divergence in a naïve low-temperature expansion in small fluctuations. To illustrate, let us start from an arbitrary ground state ordered at wavevector $\mathbf{Q}$, with a corresponding spin configuration $\overline{\mathbf{S}}_i$, and expand the Hamiltonian in fluctuations $\delta\mathbf{S}_i = \mathbf{S}_i - \overline{\mathbf{S}}_i$. To leading order in temperature the thermally averaged fluctuation amplitude, by equipartition, is given by

$$\langle \delta\mathbf{S}_i^2 \rangle \sim T \int \frac{d^3\mathbf{q}}{\omega_0^2(\mathbf{q})} \to \infty, \tag{2}$$

which diverges due to the infinite number of zeros in $\omega_0(\mathbf{q})$. However, since only a finite number of these zero-frequency modes, the "Goldstone modes", are guaranteed by symmetry, thermal fluctuations can lift the remaining "accidental" zeros, potentially stabilizing an ordered state.

This stabilization indeed occurs. Interestingly, modifications to $\omega_0(\mathbf{q})$ by thermal fluctuations are non-perturbative in temperature. We therefore obtain the leading corrections for $T \ll \Theta_{CW}$ within a self-consistent treatment as described in the Supplementary Material. Provided $J_1 \neq 0$, we find that for $\mathbf{q}$ on the spiral surface the frequencies become

$$\omega_T^2(\mathbf{q}) = \omega_0^2(\mathbf{q}) + T^{2/3}\Sigma(\mathbf{q}), \tag{3}$$

where $\Sigma(\mathbf{q})$ is temperature-independent and generically vanishes *only* at the spiral wavevectors $\pm\mathbf{Q}$, which are precisely the locations of the Goldstone modes. Thus entropy indeed lifts the surface degeneracy, which cures the divergence in Eq. (2) and stabilizes long-range order. Nevertheless, the order is in a sense "unconventional" in that anomalies in thermodynamic quantities

appear due to the non-analytic temperature dependence in Eq. (3). In particular, the classical specific heat at low temperatures scales as

$$C_v^{\text{classical}}(T) = A + BT^{1/3}, \tag{4}$$

with A and B constants. A crude quantum treatment, obtaining the magnon spectrum $\epsilon(\mathbf{q}) = \hbar\omega_T(\mathbf{q})$ by quantizing the classical modes of Eq.(3), predicts the fractional power-law $C_v^{\text{quantum}}(T) \sim T^{7/3}$. This is intriguingly reminiscent of the approximately $T^{2.5}$ behavior observed in $CoAl_2O_4$ [16] and related materials [17].

We now address *which* state thermal fluctuations select. Although the energy E associated with each wavevector on the spiral surface is identical, their entropy S and hence *free energy* $F = E - TS$ generally differ. Typically, entropy favors states with the highest density of nearby low-energy excitations. To compute the free energy at low temperatures, it suffices to retain terms in the Hamiltonian which are quadratic in fluctuations about a state ordered at wavevector $\mathbf{Q}$. The free energy can then be computed numerically for each $\mathbf{Q}$ on the surface. The results for select J_2/J_1 are illustrated in Fig. 2, where the surface is colored according to the magnitude of the free energy (blue is high, red is low, and the global minima are green). As indicated in Fig. 3(a), the free energy minima occur at the following locations as J_2/J_1 varies: (i) along the (q, q, q) directions for $1/8 < J_2/J_1 \leq 1/4$ as in Fig. 2(a); (ii) at the six wavevectors depicted in Fig. 2(b) located around each "hole" in the surface for $1/4 < J_2/J_1 \lesssim 1/2$; (iii) along the $(q, q, 0)$ directions when $1/2 \lesssim J_2/J_1 \lesssim 2/3$; and (iv) at four points centered around each $(q, 0, 0)$ direction as in Fig. 2(c) for larger J_2. Eventually the latter points converge precisely onto the $(q, 0, 0)$ directions, where the nearest-neighbor FCC antiferromagnet is known to order [12].

We next turn to the evolution with increasing temperature, for which we rely on extensive Monte Carlo simulations and analytic arguments. As one introduces frustration via J_2, it is natural to expect a sharply reduced transition temperature T_c relative to Θ_{CW}, and this is indeed borne out in our simulations. Figure 3 (a) illustrates T_c versus J_2/J_1 computed numerically for systems with up to $N = 4096 = 8 \times 8^3$ spins. In the Néel phase, a sharp decrease in T_c is evident upon increasing J_2. As an interesting aside, for J_2/J_1 just above 1/8 *two* ordering transitions appear below the paramagnetic phase. This occurs due to thermal stabilization of the Néel phase slightly beyond the value of $J_2/J_1 = 1/8$; the reentrant Néel order appears below the dashed black line in Fig. 3(a). More interestingly, T_c clearly remains non-zero for $J_2/J_1 > 1/8$, in agreement with the preceding order-by-disorder analysis. Throughout this region, the transition is strongly first order.

Due to the strong suppression of T_c when $J_2/J_1 > 1/8$, one can explore a broad range of the spin liquid regime in the paramagnetic state above T_c and below $|\Theta_{CW}|$. Interestingly, the spiral surface, as well as entropic free-energy corrections, can be directly probed via the spin structure factor. This is illustrated in Fig. 3(b), which displays the structure factor $S^{AA}(\mathbf{q})$ corresponding to spin correlations on one of the two FCC sublattices. (Experimentally, $S^{AA}(\mathbf{q})$ can be obtained from the full structure factor as described in the Supplementary Material.) The data correspond to $N = 13824$ spins with $J_2/J_1 = 0.85$, relevant for $MnSc_2S_4$ as discussed below, at a temperature just above T_c. Here we plot only momenta contributing the highest 44% intensity (blue points have lower intensity, red higher, and green corresponds to the maxima); the similarity to Fig. 2(c) is rather striking. The free-energy splitting manifest here persists up to $T \approx 1.3T_c$, while the surface itself remains discernible out to $T \approx 3T_c$ (see Fig.4(a)). The spiral ground states evidently dominate the physics for $T_c \lesssim T \lesssim 3T_c$, so that this regime can be appropriately characterized as a "spiral spin liquid".

To quantify the behavior in this regime analytically, we calculated the structure factor within the "spherical" approximation, in which the unit-magnitude constraint on each spin is relaxed to $\sum_i |\mathbf{S}_i|^2 = N$. The classical spin liquids in kagome [21] and pyrochlore [3] antiferromagnets are known to be well-described by this scheme. Here, we find that the structure factor is similarly peaked on the spiral surface, with a width $\xi^{-1} \sim k_B T$ that agrees quantitatively with the fitted value from numerics. Moreover, the complete three-dimensional structure factor data collapse onto a (known) one-dimensional curve when plotted versus the variable $\Lambda(\mathbf{q}) = 2\sqrt{\cos^2 \frac{q_x}{4} \cos^2 \frac{q_y}{4} \cos^2 \frac{q_z}{4} + \sin^2 \frac{q_x}{4} \sin^2 \frac{q_y}{4} \sin^2 \frac{q_z}{4}}$. As illustrated in Fig. 4(a) for $J_2/J_1 = 0.85$, the numerical data conform well to this prediction, essentially throughout the paramagnetic phase except very near T_c where thermal fluctuations dramatically split the free energy along the surface. Note that the red analytical curves contain only a single fitting parameter, corresponding to an unimportant overall scaling.

Finally, we discuss implications for experiments, focusing on the well-characterized material $MnSc_2S_4$. Below $T_{N1} = 2.3$ K, experiments observe long-range spiral order with wavevector $\mathbf{Q}_{exp} \approx 2\pi(3/4, 3/4, 0)$, coexisting with pronounced correlations with wavevector magnitude $Q_{\text{diff}} \approx 2\pi$ that persist to well above T_{N1} [20, 22]. A second transition occurs at $T_{N2} = 1.9$ K, below which the latter correlations are greatly suppressed. Assuming $\mathbf{Q}_{exp}$ lies near the spiral surface, we estimate that $J_2/J_1 \approx 0.85$ for this material. By comparing the structure of the spiral ground state ordered at $\mathbf{Q}_{exp}$ with the experimentally determined spin structure [20], we further deduce that J_1 must be ferromagnetic (*i.e.*, $J_1 < 0$) in $MnSc_2S_4$. One can then extract the magnitudes of the exchange constants from the measured Curie-Weiss temperature $\Theta_{CW} \approx -22.1$ K; we obtain $J_1 \approx -1.2$ K and $J_2 \approx 1.0$ K. According to the numerical results of Fig. 3, the predicted ordering temperature for these parameters is $T_c \approx 2.4$K.

Obtaining a detailed comparison to the *low-temperature* experimental order requires perturbing our parent Hamiltonian. Quite

generally, these corrections inevitably overwhelm the entropic free energy splittings discussed above at sufficiently low temperature, since the latter vanish as $T \to 0$. Happily, the simplest correction—a small antiferromagnetic third-neighbor exchange J_3—favors the observed $(q, q, 0)$ spiral direction. The close proximity of the calculated T_c for $J_3 = 0$ to the experimental T_{N1} suggests that J_3 should indeed be small. For sufficiently small J_3, the entropic splittings will outweigh this energetic correction at higher temperatures, giving way to an intermediate phase with long-range spiral order along the entropically favored (approximately) $(q, 0, 0)$ directions. As J_3 increases (but remains small), this order-by-disorder phase will be weakened and eventually removed, leaving only the more robust spiral spin liquid correlations above T_c. The Q_{diff} scattering deduced from powder neutron experiments is consistent with weak order-by-disorder as well our predictions for the spiral spin liquid, and further single-crystal experiments are needed to distinguish between these scenarios. For comparison with the latter, in Fig. 4(b) we display the numerically powder averaged spherical model structure factor $S_{\text{ave}}(Q)$ for $J_3 = |J_1|/20$ at several temperatures above T_c. This reproduces well the experimental diffuse correlations near Q_{diff} as temperature smears the J_3 splitting. In short, the "competing order" observed at intermediate temperatures is precisely in line with theoretical expectations in our framework, and thus in our view provides convincing experimental evidence for our model's relevance to the physics of $MnSc_2S_4$.

Looking forward, many other materials are anticipated to be well-described by our model, from the marginally frustrated $CoRh_2O_4$ and $MnAl_2O_4$ with $f \approx 1.2$ and $f \approx 3.6$, respectively, to the highly frustrated $CoAl_2O_4$. Existing measurements place a lower bound on the frustration parameter for $CoAl_2O_4$ of around 10-20; a broad peak in the specific heat evidently preempts a sharp ordering transition in current samples [15, 16]. As described in the Supplementary Material, the available low-temperature powder neutron data together with the large frustration parameter are consistent with this material residing in the region $J_2/J_1 \approx 1/8$, where the spiral surface begins to develop. Experiments with increased sample purity would likely allow for a more direct comparison. Regarding future experiments more generally, most exciting would be single crystal neutron data, which would allow a much more direct and detailed comparison of theory and experiment. One could carry out an analysis similar to the one performed for the structure factor in our Monte Carlo simulations, as detailed in the Supplementary Material. In this way, one might directly observe the spiral surface in the spiral spin liquid regime and perhaps find the first unambiguous experimental signatures of order-by-disorder, both of which would be truly remarkable.

Supplementary Material

LOW TEMPERATURE

Ground states

To find the ground states of our parent theory, it is useful to diagonalize the Hamiltonian by transforming to momentum space. Since the diamond lattice is an FCC Bravais lattice with a two-site basis, this reveals two bands with energies

$$\epsilon_\pm(\mathbf{q}) = 4J_2[\Lambda^2(\mathbf{q}) - 1] \pm 2J_1\Lambda(\mathbf{q}). \tag{5}$$

Here and below we assume antiferromagnetic $J_{1,2} > 0$; the function $\Lambda(\mathbf{q})$ is defined by

$$
\begin{aligned}
\Lambda(\mathbf{q}) &= 2[\cos^2(q_x/4)\cos^2(q_y/4)\cos^2(q_z/4) \\
&+ \sin^2(q_x/4)\sin^2(q_y/4)\sin^2(q_z/4)]^{1/2}
\end{aligned} \tag{6}
$$

as provided in the main text. The minimum eigenvalue is realized in the lower band $\epsilon_-(\mathbf{q})$, and occurs at a single point ($\mathbf{q} = \mathbf{0}$) for $J_2/J_1 < 1/8$ but on a two-dimensional *surface* in momentum space for larger J_2/J_1.

Our strategy is to explicitly construct states that contain Fourier weight only at the minimum eigenvalue, *and* simultaneously satisfy the unit-vector constraint for each spin. Such states are guaranteed to be ground states, as mixing any other Fourier components necessarily increases the energy. For $J_2/J_1 < 1/8$ this prescription gives the expected Néel phase as the unique ground state (apart from global spin rotations). For larger J_2/J_1 one can construct highly degenerate spiral ground states, each characterized by a single wavevector lying on the "spiral surface" corresponding to the minimum of $\epsilon_-(\mathbf{q})$. Denoting the two FCC sublattices by A and B and the lattice site positions by $\mathbf{r}_j$, the spiral ground states explicitly take the form

$$\mathbf{S}_j^{A/B} = \mp[\hat{\mathbf{x}}\cos\varphi_j^{A/B} + \hat{\mathbf{y}}\sin\varphi_j^{A/B}] \tag{7}$$

$$\varphi_j^{A/B} = \mathbf{q} \cdot \mathbf{r}_j \pm \theta(\mathbf{q})/2, \tag{8}$$

with any wavevector $\mathbf{q}$ on the spiral surface. We have assumed a spiral in the x-y plane, though any two orthonormal unit vectors above will clearly do. The angle $\theta(\mathbf{q})$ determines the relative phase shift between the A and B sublattices, and is given by the argument of

$$\cos\left(\frac{q_1}{4}\right)\cos\left(\frac{q_2}{4}\right)\cos\left(\frac{q_3}{4}\right) - i\sin\left(\frac{q_1}{4}\right)\sin\left(\frac{q_2}{4}\right)\sin\left(\frac{q_3}{4}\right) . \tag{9}$$

(Note that for ferromagnetic $J_1 < 0$, the corresponding ground states are obtained by reversing the spins on one FCC sublattice.)

While this does not exhaust all possible ground states, others occur only at special values of J_2/J_1 or contribute only a finite discrete set and are thus anticipated to be less important than these generic spirals. For instance, a discrete set of ground states constructed from wavevectors on the surface differing by half a reciprocal lattice vector can be realized over a range of J_2/J_1.

Local stability

Henceforth we focus on the regime $J_2/J_1 > 1/8$. Given the massive spiral ground state degeneracy here, the question of stability of long-range order becomes quite delicate. The goal of this subsection is to demonstrate that *entropy* stabilizes long-range order at finite temperature by lifting the degeneracy in the free energy along the spiral surface, *i.e.*, the system undergoes a thermal order-by-disorder transition.

To this end, we start from an arbitrary ground state ordered at momentum $\mathbf{Q}$ with a spin configuration $\overline{\mathbf{S}}_j$ and expand in fluctuations by writing

$$\mathbf{S}_j = \vec{\pi}_j + \overline{\mathbf{S}}_j\sqrt{1 - \vec{\pi}_j^2} . \tag{10}$$

The fluctuation field $\vec{\pi}_j$ is constrained such that $\overline{\mathbf{S}}_j \cdot \vec{\pi}_j = 0$ so that the unit-vector constraint remains satisfied. After computing the Jacobian for the variable transformation, the partition function becomes

$$\begin{aligned}
\mathcal{Z} &= \int \mathcal{D}\mathbf{S}\, e^{-\beta H} \prod_{\mathbf{r}} \delta[\mathbf{S}_j^2 - 1] \\
&= \int \mathcal{D}\vec{\pi}\, e^{-\beta H} \prod_{\mathbf{r}} \left[1 - \vec{\pi}_j^2\right]^{-1/2} .
\end{aligned} \tag{11}$$

An expansion in small fluctuations can be controlled at low temperatures. Assuming the spins $\overline{\mathbf{S}}_j$ lie in the x-y plane, we parametrize the fluctuations as follows,

$$\vec{\pi}_j = \hat{\mathbf{z}}\phi_j + [\hat{\mathbf{z}} \times \overline{\mathbf{S}}_j]\chi_j , \tag{12}$$

thereby automatically satisfying the constraint $\overline{\mathbf{S}}_j \cdot \vec{\pi}_j = 0$. The partition function can now be expressed in terms of an action,

$$\mathcal{Z} = \int \mathcal{D}\phi \mathcal{D}\chi\, e^{-S} . \tag{13}$$

Retaining the leading corrections to the Gaussian theory, the action can be written as $S = S_2 + S_3 + S_4$, where

$$\begin{aligned}
\mathcal{S}_2 &= \frac{\beta}{2}\sum_{ij}\left[\tilde{J}_{ij}\phi_i\phi_j + W_{ij}\chi_i\chi_j\right] - \frac{1}{2}\sum_j[\phi_j^2 + \chi_j^2] \\
\mathcal{S}_3 &= \frac{\beta}{2}\sum_{ij}K_{ij}\phi_i\left(\phi_j^2 + \chi_j^2\right) \\
\mathcal{S}_4 &= \frac{\beta}{8}\sum_{ij}W_{ij}\left(\phi_i^2 + \chi_i^2\right)\left(\phi_j^2 + \chi_j^2\right) .
\end{aligned} \tag{14}$$

Here $\tilde{J}_{ij}$ is simply the exchange matrix J_{ij} shifted by a constant, such that all the eigenvalues are non-negative and the ground state space corresponds to the kernel of this matrix. We have also defined the matrices $W_{ij} = \tilde{J}_{ij}\left(\overline{\mathbf{S}}_j \cdot \overline{\mathbf{S}}_i\right)$ and $K_{ij} = \tilde{J}_{ij}\left[\hat{z} \cdot \left(\overline{\mathbf{S}}_j \times \overline{\mathbf{S}}_i\right)\right]$. The Jacobian factor has been absorbed into the action, giving rise to the last summation in S_2.

According to Eq. (12), fluctuations out of the spiral plane are described by ϕ_j, while χ_j describes in-plane fluctuations. Long-range order will occur if these fluctuations can always be made small by going to sufficiently low temperature. The

latter generically have only a single gapless mode, corresponding to the symmetry-required Goldstone mode at zero momentum. Consequently, fluctuations in χ_j are clearly well-behaved at low temperature. Subtleties with long-range order arise from the ϕ_j fluctuations, which connect the degenerate ground states. At the Gaussian level and to leading order in temperature, the ϕ_j propagator is

$$G_{ij}^0 = \langle \phi_j \phi_i \rangle_0 = \tilde{J}_{ij}^{-1}. \tag{15}$$

In momentum space, the associated normal mode frequencies $\omega_0(\mathbf{q})$ and $\omega_1(\mathbf{q})$ are defined by

$$\omega_{0,1}^2(\mathbf{q}) \equiv \epsilon_\mp(\mathbf{q}) - \epsilon_-^{\min}, \tag{16}$$

where $\epsilon_-^{\min}$ corresponds to the minimum value of $\epsilon_-(\mathbf{q})$. It follows that the fluctuation amplitude for ϕ_j naively *diverges*,

$$\langle \phi_j^2 \rangle_0 \sim T \int_{\mathbf{q}} \frac{1}{\omega_0^2(\mathbf{q})} \to \infty \,, \tag{17}$$

since $\omega_0(\mathbf{q})$ vanishes for any $\mathbf{q}$ on the spiral surface due to the continuous ground state degeneracy.

Higher-order corrections in temperature, however, lift the surface degeneracy, thus curing the above divergence and stabilizing long-range order. Perturbation theory in temperature suffers similar divergences as found above, and hence we employ a self-consistent treatment to obtain corrections to the ϕ_j fluctuations. The ϕ_j propagator obtained from the full action S defined above is

$$G_{ij} = \langle \phi_j \phi_i \rangle = \left[\tilde{J}_{ij} + \tilde{\Sigma}_{ij} \right]^{-1}, \tag{18}$$

where $\tilde{\Sigma}_{ij}$ is the *self-energy*. In particular, we are interested in the self-energy correction to $\omega_0(\mathbf{p})$, which we will denote $\tilde{\Sigma}(\mathbf{p})$, for momenta $\mathbf{p}$ along the spiral surface.

To proceed, we first assume that thermal fluctuations indeed break the surface degeneracy, and then find the leading corrections self-consistently. More specifically, we assume that $\tilde{\Sigma}(\mathbf{p}) \sim T^\alpha \Sigma(\mathbf{p})$, where $\alpha < 1$, $\Sigma(\mathbf{p})$ is temperature-independent, and $\Sigma(\pm \mathbf{Q}) = 0$; the last condition simply asserts that the symmetry-required Goldstone modes at the ordering wavevectors are preserved. With these assumptions, we obtain a self-consistent equation of the form

$$\tilde{\Sigma}(\mathbf{k}) = T \int_{\mathbf{q}} \Gamma(\mathbf{q}, \mathbf{k}) G(\mathbf{q}) \,, \tag{19}$$

with $G(\mathbf{q}) = \left[\omega_0^2(\mathbf{q}) + \tilde{\Sigma}(\mathbf{q}) \right]^{-1}$ and $\Gamma(\mathbf{q}, \mathbf{k})$ temperature-independent. At low-temperatures, the integral is dominated by momenta near the spiral surface due to the propagator $G(\mathbf{q})$. By contrast, the function $\Gamma(\mathbf{q}, \mathbf{k})$ is well behaved and does not lead to any additional singular behavior. Hence it is sufficient to replace $\Gamma(\mathbf{q}, \mathbf{k}) \to \Gamma(\mathbf{q}_s, \mathbf{k})$ under the integral, where $\mathbf{q}_s$ lies precisely on the surface in the direction of $\mathbf{q}$. One can show that $\Gamma(\mathbf{q}_s, \pm \mathbf{Q}) = 0$, so that the Goldstone modes are indeed preserved within our self-consistent treatment. Furthermore, one can approximate $G(\mathbf{q}) \approx \left[\kappa (q - q_s)^2 + T^\alpha \Sigma(\mathbf{q}) \right]^{-1}$ in the integrand. The temperature dependence can then be scaled out of the integral, implying a power $\alpha = 2/3$ consistent with our assumptions.

The divergent fluctuations are thus cured by the onset of a thermally induced splitting $\Delta \sim T^{2/3}$ along the spiral surface. Consequently, ordering at finite temperature will occur, despite the massive ground state degeneracy.

Global selection

In the previous subsection we found that thermal fluctuations stabilize long-range order at finite temperature. Here we address the more specific (and simpler) question of which state among the degenerate set is favored. At finite temperature, entropy selects the states minimizing the free energy $F = E - TS$ (E is energy, S entropy), which usually are those with the highest density of nearby low-energy states. Let us start from an arbitrary spiral with ordering wavevector $\mathbf{Q}$, and expand in fluctuations as outlined in the previous subsection. At low temperatures, for our purpose here it suffices to retain only the first two terms in the Gaussian action S_2. Integrating over the fluctuation fields, we then obtain the leading T- and $\mathbf{Q}$-dependent contribution to the free energy,

$$\begin{aligned} F(\mathbf{Q}) &= -T \ln(\mathcal{Z}) \\ &\sim T \left(Tr \left[\ln(\tilde{J}/2\pi T) \right] + Tr \left[\ln(W(\mathbf{Q})/2\pi T) \right] \right) \,, \end{aligned} \tag{20}$$

where $\hat{J}, \hat{W}$ denote the matrices defined in the previous subsection and we have explicitly labeled the $\mathbf{Q}$-dependence in $\hat{W}$. The first term is $\mathbf{Q}$-independent and thus does not distinguish the states on the spiral surface. This is accomplished, however, by the second term, which can be easily computed numerically as a function of $\mathbf{Q}$ to obtain the global free energy minima. The resultant free-energy splittings are illustrated through the coloring of the surfaces in Fig. 2 of main text. Also, we display in Fig. 5 the free energy along high-symmetry directions as a function of J_2/J_1. Here, 111^* refers to six momenta located along the "holes" which develop in the surface for $J_2/J_1 > 1/4$, and 100^* corresponds to four momenta located around the 100 directions (see main text).

Specific heat

The anomalous low temperature dependence of the free energy will manifest itself in thermodynamic quantities. In this section we show explicitly how the specific heat varies with temperature in this regime.

The heat capacity $C_v = -T \left(\frac{\partial^2 F}{\partial T^2} \right)_{V,N}$ can be found from our low temperature expression for the free energy. Including only the anomalous part of the self energy, while neglecting all analytic corrections higher order in T, we modify (20) to

$$
\begin{aligned}
F \sim & T \left(Tr \left[\ln[(\tilde{J} + \tilde{\Sigma})/2\pi T] \right] + Tr \left[\ln(W(\mathbf{Q})/2\pi T) \right] \right) \\
\sim & - A_1 T \ln(T) + A_2 T + T \int_{\mathbf{q}} \ln[(\omega_0^2(\mathbf{q}) + T^{2/3}\Sigma(\mathbf{q}))] .
\end{aligned}
\tag{21}
$$

To find the behavior of the integral at low temperatures, it is useful to consider

$$
\frac{\partial(F/T)}{\partial T} \sim -\frac{A_1}{T} + \frac{2}{3} T^{-1/3} \int_{\mathbf{q}} \frac{\Sigma(\mathbf{q})}{(\omega_0^2(\mathbf{q}) + T^{2/3}\Sigma(\mathbf{q}))}
\tag{22}
$$

scaling temperature out of the momentum integral on the right hand side. In the same manner we proceeded for the integral in (19), we find $\int_{\mathbf{q}} \frac{\Sigma(\mathbf{q})}{(\omega_0^2(\mathbf{q}) + T^{2/3}\Sigma(\mathbf{q}))} \sim T^{-1/3}$ so that $\frac{\partial(F/T)}{\partial T} \sim -\frac{A_1}{T} + \frac{2}{3} T^{-2/3} B$. The low temperature form of the free energy is

$$
F \sim -A_1 T \ln(T) + A_2 T + A_3 T^{4/3}
\tag{23}
$$

where $A_{1,2,3}$ are constants. From this form it follows that the heat capacity is

$$
C_v^{\text{classical}}(T) = A + B T^{1/3} .
\tag{24}
$$

HIGH TEMPERATURE

This section is concerned with analytically describing the spin correlations at temperatures above T_c. Remarkably, these allow one to probe directly the underlying ground state surface in the "spiral spin liquid" regime occurring over a broad temperature range. In the disordered phase above T_c, the spins fluctuate strongly, and it is reasonable that the unit length constraint on the individual spins can be relaxed. Hence we employ the "spherical" approximation, replacing the local unit-vector spin constraint with the global constraint $\sum_j \mathbf{S}_j^2 = N$, N being the total number of sites. The spin correlations determined via Monte Carlo numerics are described *quantitatively* within this scheme, except very near T_c where entropic effects are dramatic.

The partition function for this model is

$$
\mathcal{Z} = \int \mathcal{D}\mathbf{S} d\lambda e^{-\beta H - i\lambda(\sum_j \mathbf{S}_j^2 - N)} ,
\tag{25}
$$

where λ is a Lagrange multiplier enforcing the global constraint. To proceed we employ a saddle-point approximation, replacing $i\lambda \to \beta\Delta(T)/2$, where $\Delta(T)$ is the saddle-point value to be determined. The spin correlation function is then

$$
\langle \mathbf{S}_i \mathbf{S}_j \rangle = 3T \left[J_{ij} + \delta_{ij}\Delta(T) \right]^{-1} .
\tag{26}
$$

Upon integrating over the spins, one obtains the saddle point equation for $\Delta(T)$:

$$
\frac{1}{T} = \frac{3}{2} \int_{\mathbf{q}} \sum_{j=0,1} \frac{1}{\omega_j^2(\mathbf{q}) + \Delta(T)} .
\tag{27}
$$

Equations (26) and (27) together determine the spherical model spin correlations. In particular, the momentum-space correlation function for spins on the same FCC sublattice is given by

$$S^{AA}(\mathbf{q}) \sim T\left[\frac{1}{\omega_0^2(\mathbf{q}) + \Delta(T)} + \frac{1}{\omega_1^2(\mathbf{q}) + \Delta(T)}\right], \tag{28}$$

while the correlation between spins on opposite FCC sublattices is

$$S^{AB}(\mathbf{q}) \sim Te^{-i\theta(\mathbf{q})}\left[\frac{-1}{\omega_0^2(\mathbf{q}) + \Delta(T)} + \frac{1}{\omega_1^2(\mathbf{q}) + \Delta(T)}\right]. \tag{29}$$

The full structure factor, as measured in experiment, is

$$S(\mathbf{q}) = S^{AA}(\mathbf{q}) + \mathrm{Re}[S^{AB}(\mathbf{q})]. \tag{30}$$

Notice that the spin correlation $S^{AA}(\mathbf{q})$ depends on momentum only through the function $\Lambda(\mathbf{q})$. ($\mathbf{S}^{AB}(\mathbf{q})$ has additional momentum dependence through $\theta(\mathbf{q})$.) Hence it is highly desirable to isolate this contribution, as $S^{AA}(\mathbf{q})$ collapses onto a known one-dimensional curve when plotted versus $\Lambda(\mathbf{q})$. We have extracted $S^{AA}(\mathbf{q})$ in our Monte Carlo simulations for $J_2/J_1 = 0.2, 0.25, 0.4, 0.6, 0.85$, and indeed find that in all cases for $T > T_c$ the correlation function data collapse well when plotted versus $\Lambda(\mathbf{q})$. Furthermore, in all these cases one finds *quantitative* agreement with the analytic result Eq. (28), with only a single fitting parameter corresponding to an overall scaling. The excellent agreement obtained here is illustrated in the main text for $J_2/J_1 = 0.85$. The peaks in these figures correspond to values of $\Lambda(\mathbf{q})$ defining the spiral surface, thus implying that spin configurations near the surface dominate the physics. This is the spiral spin liquid regime.

Naively, isolating $S^{AA}(\mathbf{q})$ experimentally appears more difficult. Fortunately, this component can be extracted from the full structure factor by using the fact that $\theta(\mathbf{q}) = \theta(\mathbf{q} + \mathbf{K}) + \pi$, where $\mathbf{K} = 4\pi(1, 0, 0)$ is a reciprocal lattice vector. This leads to the useful identity

$$S^{AA}(\mathbf{q}) = \frac{1}{2}[S(\mathbf{q}) + S(\mathbf{q} + \mathbf{K})]. \tag{31}$$

It would be extremely interesting to perform a similar analysis on experimental neutron scattering data, which would require single crystals. The spiral surface could then be extracted quite simply as follows. Display momenta in the first Brillouin zone corresponding to the highest intensity points within some threshold—the surface is mapped out when an appropriate threshold is chosen. Such an analysis was carried out for the Monte Carlo structure factor, the result of which are shown in the main text.

Obtaining single crystal samples is often challenging, so it is highly desirable (and of current experimental relevance) to have a way of detecting the spiral surface in neutron data for powder samples. The full structure factor can be numerically "powder-averaged" by performing an angular integration for a given wavevector magnitude Q:

$$S_{\mathrm{ave}}(Q) = \int \sin\theta d\theta d\varphi S(\mathbf{Q}), \tag{32}$$

where θ and φ are polar and azimuthal angles specifying the direction of $\mathbf{Q}$. The spiral surface is then indirectly revealed as a peak in $S_{\mathrm{ave}}(Q)$ over the range of Q for which the surface occurs. Existing neutron data for $MnSc_2S_4$ powder samples indeed reveal a broad peak in the structure factor in agreement with our predictions for the spiral spin liquid regime. Furthermore, excellent agreement with powder neutron data for $CoAl_2O_4$ can be obtained by assuming that $J_2/J_1 \approx 1/8$ for this material. Fig. 6 displays the predicted powder-averaged structure factor, which exhibits peaks and valleys that correspond well to those observed experimentally [23]. The low-T_c in this vicinity of J_2/J_1 is further consistent with the large frustration parameter observed for $CoAl_2O_4$.

MONTE CARLO METHODS

In our numerical simulations of Hamiltonian we used classical Monte Carlo techniques employing a parallel tempering scheme [24] where multiple replicas of the system are simulated simultaneously over a range of temperature. Thermal equilibration can be dramatically increased by swapping replicas between neighboring temperature points. An optimal set of temperature points in the vicinity of the phase transition has been identified for each ratio of competing interactions J_2/J_1 applying a recently introduced feedback technique [25, 26]. The implementation of these algorithms was based on the ALPS libraries [27].

[1] Ramirez, A. P. Strongly geometrically frustrated magnets. *Annual Review of Materials Science* **24**, 453–480 (1994).

[2] Lee, S.-H. *et al.* Emergent excitations in a geometrically frustrated magnet. *Nature* **418**, 856 (2002).

[3] Isakov, S. V., Gregor, K., Moessner, R. & Sondhi, S. L. Dipolar spin correlations in classical pyrochlore magnets. *Physical Review Letters* **93**, 167204 (2004).

[4] Bramwell, S. T. & Gingras, M. J. P. Spin Ice State in Frustrated Magnetic Pyrochlore Materials. *Science* **294**, 1495–1501 (2001).

[5] Yamashita, Y. & Ueda, K. Spin-driven Jahn-Teller distortion in a pyrochlore system. *Physical Review Letters* **85**, 4960–4963 (2000).

[6] Veillette, M. Y., Chalker, J. T. & Coldea, R. Ground states of a frustrated spin-(1/2) antiferromagnet: Cs_2CuCl_4 in a magnetic field. *Physical Review B (Condensed Matter and Materials Physics)* **71**, 214426 (2005).

[7] Villain, J., Bidaux, R., Carton, J. P. & Conte, R. Order as an effect of disorder. *J. de Phys.* **41** (1980).

[8] Rastelli, E. & Tassi, A. Order produced by quantum disorder in the Heisenberg rhombohedral antiferromagnet. *Journal of Physics C: Solid State Physics* **20**, L303–L306.

[9] Henley, C. L. Ordering due to disorder in a frustrated vector antiferromagnet. *Phys. Rev. Lett.* **62**, 2056–2059 (1989).

[10] Chubukov, A. Order from disorder in a kagomé antiferromagnet. *Phys. Rev. Lett.* **69**, 832–835 (1992).

[11] Henley, C. L. Ordering by disorder: Ground-state selection in fcc vector antiferromagnets. *Journal of Applied Physics* **61**, 3962–3964 (1987).

[12] Gvozdikova, M. V. & Zhitomirsky, M. E. Monte Carlo study of first-order transition in Heisenberg fcc antiferromagnet. *JETP Letters* **81**, 236 (2005).

[13] Reimers, J. N. Absence of long-range order in a three-dimensional geometrically frustrated antiferromagnet. *Phys. Rev. B* **45**, 7287–7294 (1992).

[14] Moessner, R. & Chalker, J. T. Low-temperature properties of classical geometrically frustrated antiferromagnets. *Phys. Rev. B* **58**, 12049–12062 (1998).

[15] Tristan, N. *et al.* Geometric frustration in the cubic spinels MAl_2O_4 (M = Co, Fe, and Mn). *Physical Review B* **72**, 174404 (2005).

[16] Suzuki, T., Nagai, H., Nohara, M. & Takagi, H. Melting of antiferromagnetic ordering in spinel oxide $CoAl_2O_4$. *J. Phys. Cond. Matt.* (2007). To appear.

[17] Fritsch, V. *et al.* Spin and orbital frustration in $MnSc_2S_4$ and $FeSc_2S_4$. *Physical Review Letters* **92**, 116401 (2004).

[18] Smart, J. S. *Effective Field Theories of Magnetism* (W. B. Saunders Company, Philadelphia, Pennsylvania, USA, 1966).

[19] Roth, W. L. Magnetic properties of normal spinels with only A-A interactions. *J. de Phys.* **25**, 507 (1964).

[20] Krimmel, A. *et al.* Magnetic ordering and spin excitations in the frustrated magnet $MnSc_2S_4$. *Physical Review B* **73**, 014413 (2006).

[21] Garanin, D. A. & Canals, B. Classical spin liquid: exact solution for the infinite-component antiferromagnetic model on the kagomé lattice. *Phys. Rev. B* **59**, 443–456 (1999).

[22] Mucksch, M. *et al.* Multi-step magnetic ordering in frustrated thiospinel $MnSc_2S_4$. *J. Phys. Cond. Matt.* (2006). To appear.

[23] Krimmel, A., Tsurkan, V., Sheptyakov, D. & Loidl, A. Spin liquid versus spin solid in A-site spinels. *Physica B* **378-380**, 583–584 (2006).

[24] Hukushima, K. & Nemoto, K. Exchange Monte Carlo method and application to spin glass simulations. *J. Phys. Soc. Jpn.* **65**, 1604 (1996).

[25] Trebst, S., Huse, D. A. & Troyer, M. Optimizing the ensemble for equilibration in broad-histogram Monte Carlo simulations. *Phys. Rev. E* **70**, 046701 (2004).

[26] Katzgraber, H. G., Trebst, S., Huse, D. A. & Troyer, M. Feedback-optimized parallel tempering Monte Carlo. *J. Stat. Mech.* P03018 (2006).

[27] Alet, F. *et al.* The ALPS project: open source software for strongly correlated systems. *J. Phys. Soc. Jpn. Suppl.* **74**, 30 (2005).
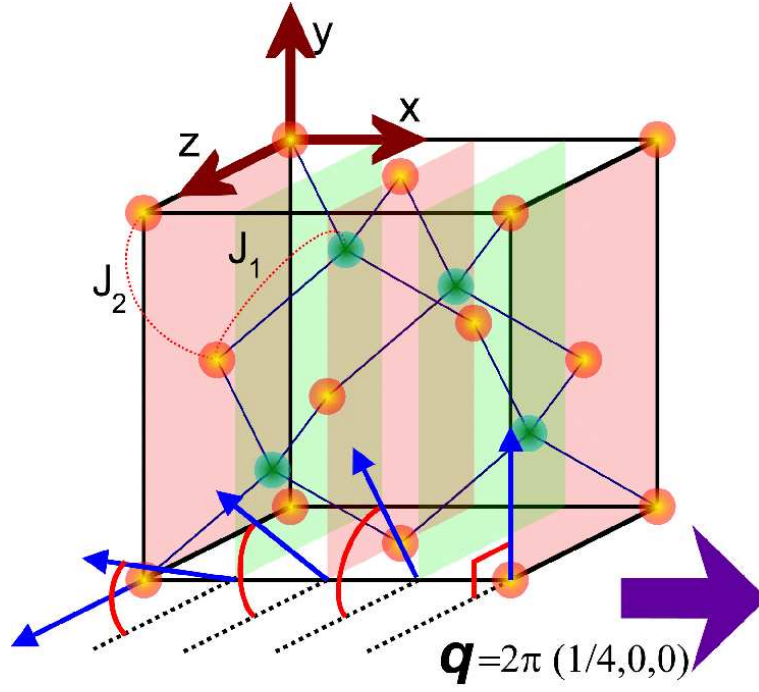
FIG. 1: The diamond lattice, composed of two interpenetrating FCC sublattices (colored orange and green). Second-neighbor antiferromagnetic exchange J_2 generates strong frustration that is compounded by the competition from the nearest-neighbor exchange J_1. For $J_2/J_1 > 1/8$, this results in a large ground state degeneracy consisting of spin spirals whose propagation wavevectors lie on a two-dimensional surface in momentum space. The arrows above denote the orientations of spins in the shaded planes for one such spiral with wavevector $\mathbf{q} = 2\pi(1/4, 0, 0)$, illustrated for ferromagnetic J_1 for clarity.

(a) (b) (c)
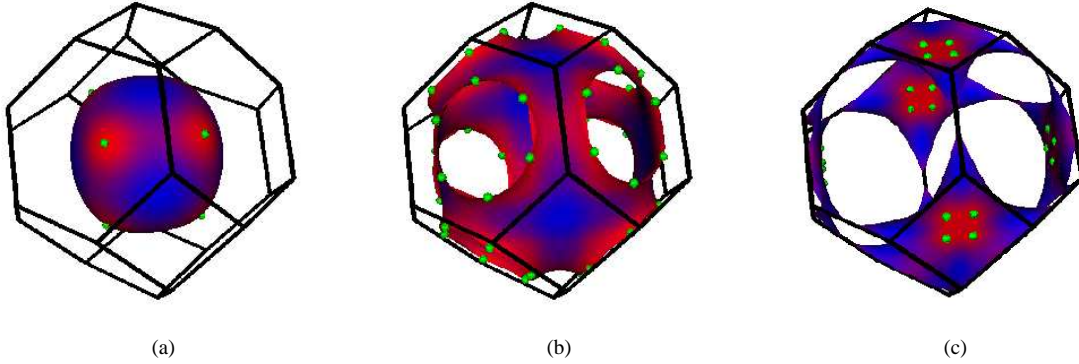
FIG. 2: "Spiral surfaces" comprising the degenerate spiral ground state wavevectors for coupling strengths J_2/J_1 of (a) 0.2, (b) 0.4, and (c) 0.85, where the last value is appropriate for $MnSc_2S_4$. Order-by-disorder occurs at finite temperature, as thermal fluctuations lift the degeneracy in the free energy. The surfaces are color-coded according to the resulting low-temperature free energy at each wavevector, with high values blue, low values red, and green the absolute minima.
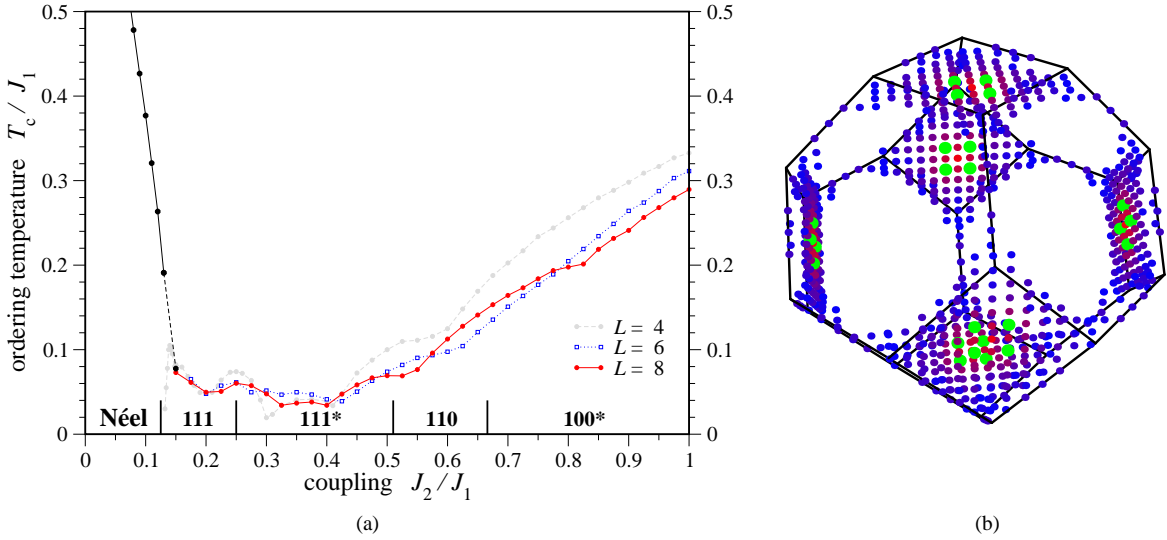
(a)

(b)

FIG. 3: (a) Numerical results for the ordering temperature T_c versus the coupling strength J_2/J_1 for systems with up to $N = 8 \times L^3 = 4096$ spins. The ordering temperature rapidly diminishes in the Néel phase upon adding frustration via J_2, and, significantly, remains finite for $J_2/J_1 > 1/8$ where the spiral surface occurs in agreement with our order-by-disorder analysis. The entropically selected ordering at low-temperatures is denoted along the horizontal axis; 111^* and 100^* refer respectively to the green points in Figs. 2(b) and (c). The "bumpy" modulations in T_c originate from an unusual finite size effect, namely variations in the number of momenta in the Brillouin zone that for the finite system approximate the spiral surface. (b) Regions of high-intensity in the magnetic structure factor in the paramagnetic phase just above T_c. The data were obtained numerically for a system with $N = 8 \times 12^3 = 13824$ spins at coupling strength $J_2/J_1 = 0.85$ appropriate for $MnSc_2S_4$. As evidenced by the remarkable similarity to Fig. 2(c), the structure factor not only clearly reveals the underlying spiral surface, but also reflects the entropic corrections to the free energy along the surface.
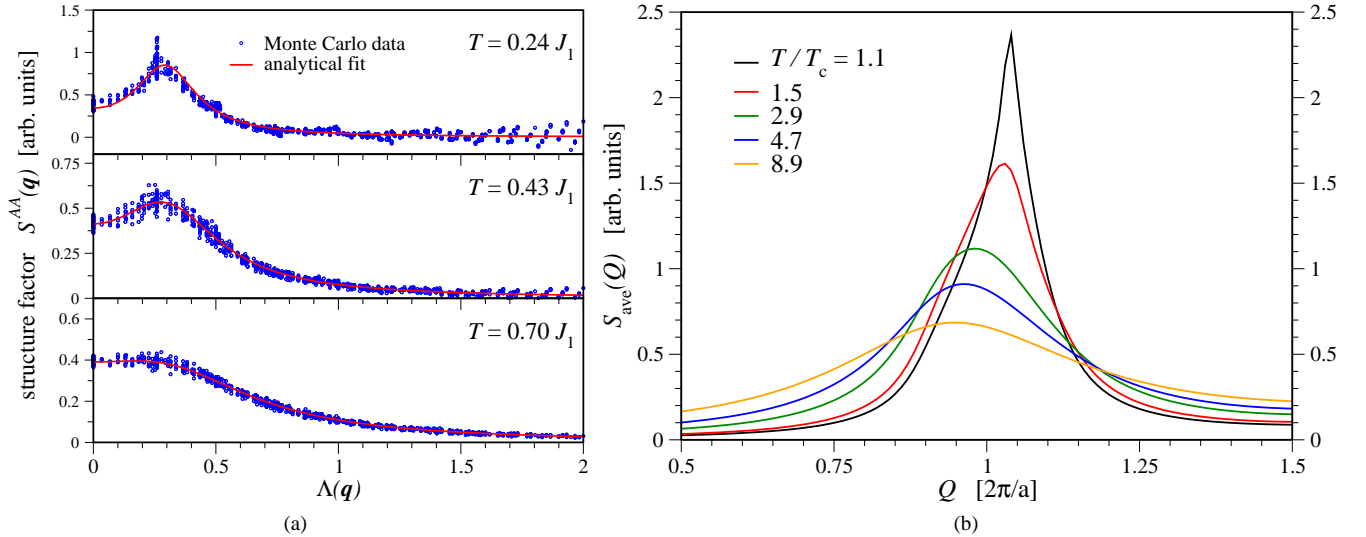

(a)

(b)

FIG. 4: (a) Structure factor data $S^{AA}(\mathbf{q})$ versus $\Lambda(\mathbf{q})$ in the paramagnetic phase with $J_2/J_1 = 0.85$, for which $T_c \approx 0.22J_1$. Essentially for all $T > T_c$, the numerical data agree quantitatively with the spherical model predictions (red curves), with one fitting parameter corresponding to an overall scaling factor. The peaks in the upper two panels correspond to points near the spiral surface, which remains discernible up to $T \approx 3T_c$. (b) Powder-averaged structure factor in the spherical model with $J_2 = -0.85J_1$ and $J_3 = -J_1/20$. The data correspond to temperatures ranging from just above T_c (black curve) to several times T_c (orange curve). Corrections due to J_3 initially dominate the signal, but are rapidly washed out as temperature increases, leaving the robust spiral spin liquid correlations. The data reproduce well the diffuse scattering around $Q_{\text{diff}} \approx 2\pi$ observed in powder neutron experiments.
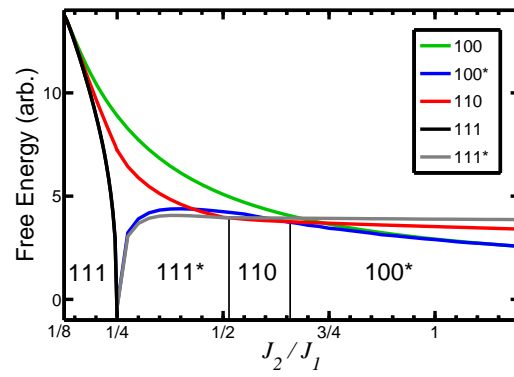
FIG. 5: Free energy versus J_2/J_1 along high-symmetry directions in the Brillouin zone.
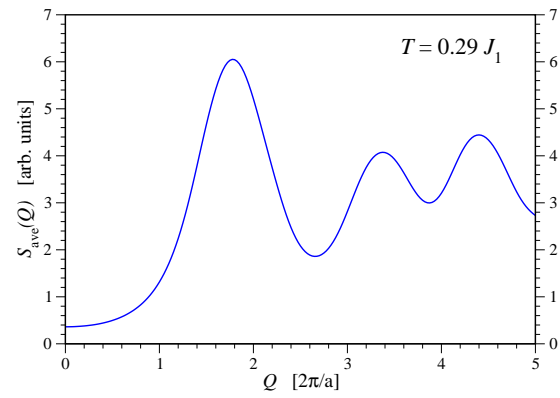

FIG. 6: Powder-averaged structure factor in the spherical model with $J_2/J_1 \approx 1/8$. The data reproduce well the diffuse scattering observed in powder neutron experiments.